NANO LETTERS

pubs.acs.org/NanoLett Letter

Atomic Scale Responses of High Entropy Oxides to Redox Environments

Zhennan Huang, Lu Wang, Tangyuan Li, Kartik Venkatraman, Yang He, Felipe Polo-Garzon, Jacob Smith, Yiheng Du, Liangbing Hu,* Zili Wu,* De-en Jiang,* and Miaofang Chi*

Cite This: https://doi.org/10.1021/acs.nanolett.4c02985 Read Online

ACCESS | Metrics & More | Article Recommendations | Supporting Information

ABSTRACT: The potential of high entropy oxides (HEOs) as high-performance energy storage materials and catalysts has been mainly understood through their bulk structures. However, the importance of their surfaces, which may play an even more critical role, remains largely unknown. In this study, we employed advanced scanning transmission electron microscopy to investigate the atomic-scale structural and chemical responses of CeYLaHfTiZrO$_x$ HEOs to high-temperature redox environments. Our observations reveal dynamic elemental and structural reconstructions in the surface of HEOs under different gas environments, contrasting with the high stability of the bulk structure. Notably, the surfaces of HEO particles consistently exhibit abundant oxygen vacancies, regardless of the redox environment. These findings indicate that HEOs offer distinct advantages in facilitating chemical and electrochemical reactions, relying on oxygen vacancies. Our results also suggest that the exceptional performance of HEOs in energy storage applications arises from surface structural and chemical adaptability.

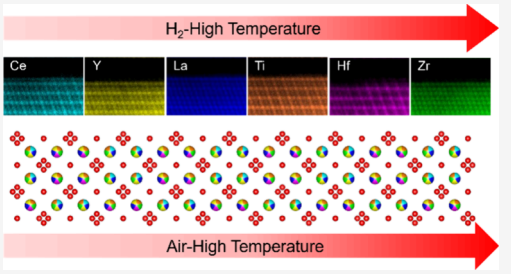

KEYWORDS: *high entropy oxide, atomic scale, surface response, redox environment*

High entropy oxides (HEOs) have recently emerged as a promising class of high-performance materials for energy storage, conversion, and catalytic applications.[1−10] Their exceptional structure stability[11,12] is believed to be the reason for their high cyclability as cathode materials for lithium and sodium ion batteries.[13−17] Additionally, their enhanced high performance in electro- and thermo-catalysis is attributed to their enhanced oxygen mobility.[18−21] HEOs have also demonstrated the ability to boost ion conductivity in solid electrolytes[22,23] and enhance the breakdown strength of dielectric capacitors[24] due to their capacity to accommodate large lattice distortions. However, our current understanding of HEOs primarily relies on knowledge of their bulk grain characteristics obtained through averaged elemental and structural measurements and calculations.[3,6,25] In contrast, little is known about their surface characteristics, which play a crucial role in chemical and electrochemical applications, let alone their responses to active environments.

In this study, we employed scanning transmission electron microscopy (STEM) imaging and spectroscopy techniques to elucidate the atomic-scale structural and elemental transformations occurring at the surfaces of HEOs under different redox environments. Our investigations utilized CeYLaHfTiZrO$_x$ as a model system and were corroborated by density functional theory (DFT) calculations. Our findings revealed that the surface and near-surface regions of the nanoparticles undergo unexpected structural and chemical reconstructions while accommodating a high density of oxygen vacancies regardless of redox environments. Additionally, we discovered that the HEO bulk exhibits a pseudorandom two-phase structure that can serve as a reservoir for oxygen vacancies.

Typical multicomponent oxide nanoparticles (NPs) with six cationic elements (Ce, Y, La, Hf, Ti, and Zr) were synthesized through the ultrafast high temperature Joule heating approach.[1,26] The as-synthesized NPs were analyzed through high-angle annular dark field (HAADF) STEM imaging and STEM-energy-dispersive X-ray spectroscopy (EDX). Figure 1a shows that all the cations and oxygen are uniformly distributed throughout the particle, indicating good elemental mixing in the HEO. The synthesis of HEOs with the same precursors through long time high temperature calcination (e.g., 1000 °C for 12 h) will result in large, irregularly shaped, branch-like structures (Figure S1). Figure S2 presents the atomically resolved structure and chemical distribution in the [001] projection of a HEO NP. From the HAADF image (Figure S2a), the interplanar spacing was measured to be 2.65 Å, matching that of the {200} planes of fluorite oxides. The corresponding atomic resolution STEM-EDX analysis (Figure S2b) depicts the uniform distributions of Ce, Y, La, Hf, Ti, and

Received: June 24, 2024
Revised: August 24, 2024
Accepted: August 26, 2024

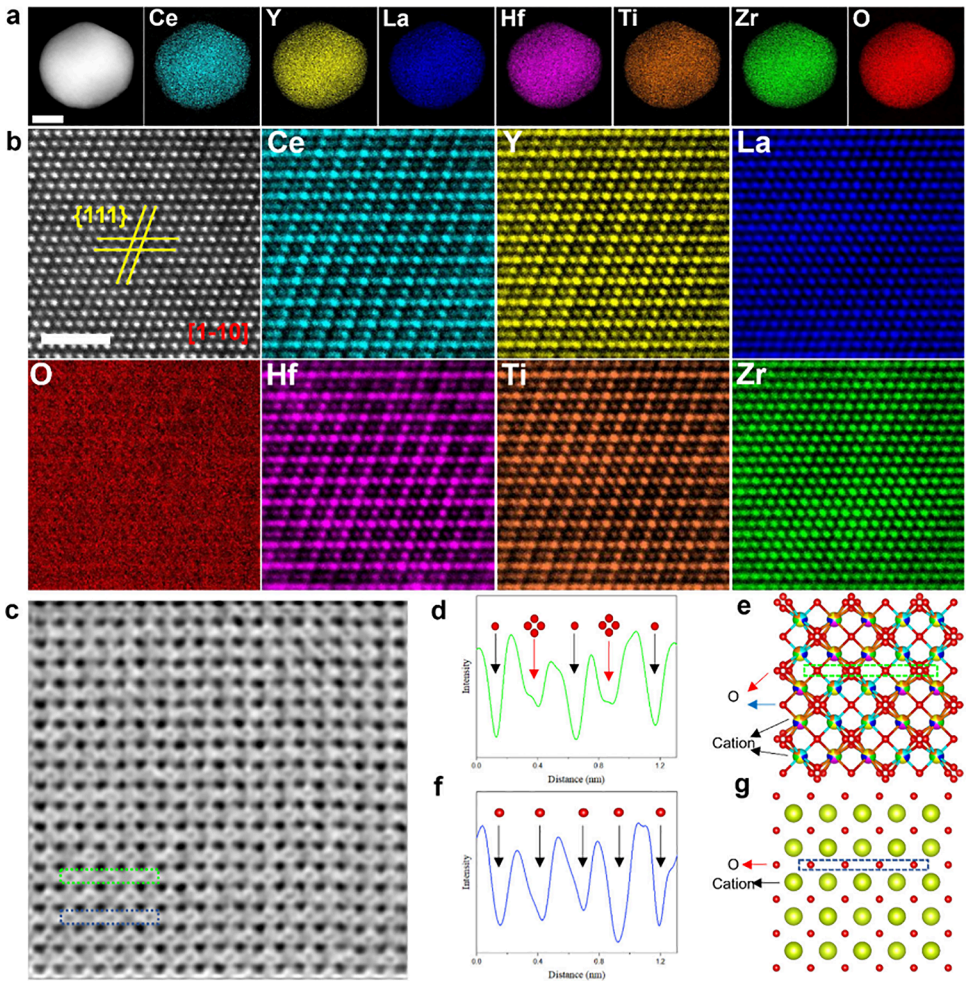

Figure 1. STEM imaging and STEM-EDX analysis reveal an unexpected, ordered structure in the CeYLaHfTiZrO$_x$ HEO particle. (a) STEM-EDX elemental maps of uniformly distributed Ce, La, Y, Ti, Zr, Hf, and O in an HEO particle, scale bar 5 nm. (b) HAADF-STEM image of an HEO NP along the [1$\bar{1}$0] projection and corresponding elemental maps of Ce, Y, La, Hf, Ti, and Zr, scale bar 2 nm. (c) ABF-STEM analysis of the HEO NPs along the [001] direction showing clear oxygen sites around cations, scale bar 1 nm. (d) Intensity line profile along the oxygen sites in the green dashed region in (c). (e) Schematic of high entropy pyrochlore viewed along the [001] zone axis. (f) Intensity line profile along the oxygen sites in the blue dashed area in (c). (g) Schematic of fluorite oxide from the [001] zone.

Zr. Localized chemical variations of individual elements are also observed. For example, Hf is rich in parts indicated by yellow arrows and poor in those indicated by white arrows. Thus, the overall cation distribution is random with local fluctuation, representing the primary features in high entropy materials that always result in more fascinating physiochemical properties than the conventional compounds.[27,28] From STEM acquisition along the [1$\bar{1}$0] zone axis (Figure 1b), the lattice spacing of the intersected planes was measured to be 3.06 Å, matching the *d*-spacing of typical fluorite oxides {111} planes. These analyses indicate that the HEO is single-phase, and its structure is most likely fluorite, as reported previously on similar composition nano-HEOs.[1,11] However, unexpected elemental ordering was unveiled in the [110] direction. As shown in the elemental maps of Figure 1b and the corresponding zoomed-in image (Figure S3a), cation species exhibit a preferential occupancy instead of the presumed random distribution. The {111} metal planes display an alternative arrangement of Ce, Y rich sites (green dots in Figure S3a) as opposed to Ti, Hf rich columns (red dots in Figure S3a), while La and Zr are well distributed at all atom positions. This occupancy preference results in two distinct metal sites in the crystal structure, which can be precisely determined from the overlay map of Ce and Hf in Figure S3b. Accordingly, a two-cation AA′$_{1-x}$O$_y$ type oxide structure might be taken into consideration. One potential crystal configuration could be pyrochlore-type oxide, general formula $A_2B_2O_7$, which is an oxygen deficient fluorite superstructure with two cation sites (A and B) periodically arranged along the [1$\bar{1}$0] projection. The corresponding unit cell structure is illustrated in Figure S4. Compared to the pristine fluorite structure (AO_2), a substantial amount of oxygen vacancies resides in the pyrochlore-type crystals.[29] Such an oxygen atom arrangement would also terminate into an organized oxygen ordering along the [001] projection.

To investigate the oxygen atom arrangements, we used an annular bright field (ABF)-STEM imaging technique, which is sensitive to light elements. Figure 1c shows a typical ABF image acquired along the [001] zone axis, which reveals that, in some regions (e.g., intensity line profile along the green dashed region (Figure 1d)), oxygen arrangement shows alternative sharper, darker contrast sites with relatively broadened, lighter contrast sites. This verifies the presence of pyrochlore structure where the oxygens are periodically arranged with well-aligned

https://doi.org/10.1021/acs.nanolett.4c02985
Nano Lett. XXXX, XXX, XXX−XXX

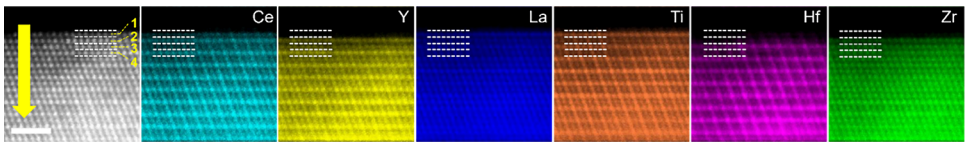

Figure 2. HAADF-STEM analysis at the very edge of the HEO particle in the [1$\bar{1}$0] zone axis (outermost four surface atomic layers marked by dashed lines) and corresponding atomic STEM-EDX maps of Ce, Y, La, Hf, Ti, and Zr. Scale bar 2 nm.

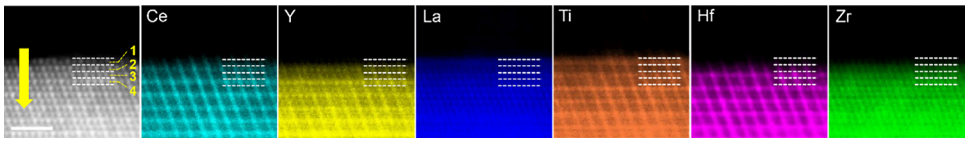

Figure 3. HAADF-STEM imaging and corresponding STEM-EDX analysis of Ce, Y, La, Ti, Hf, and Zr at the surface of the HEO particle (outermost four surface atomic layers marked by dashed lines) after 4% H_2 at 650 °C for 2 h treatment, projection [1$\bar{1}$0]. Scale bar 2 nm.

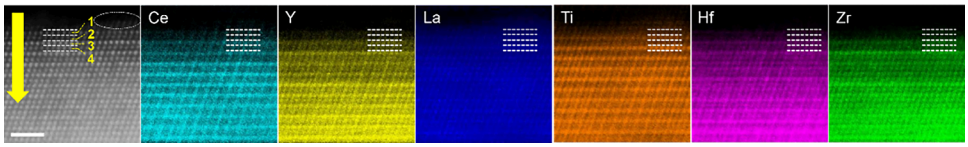

Figure 4. HAADF-STEM imaging and corresponding STEM-EDX analysis of Ce, La, Y, Ti, Zr,and Hf at the surface of the particle (outermost four surface atomic layers marked by dashed lines) after being treated in air at 650 °C for 2 h, projection [1$\bar{1}$0]. Scale bar 2 nm.

single-atom column positions and misaligned quadrilateral-shaped positions (Figure 1e). It should be noted that some regions (e.g., blue dashed areas in Figure 1c) display a random contrast of single oxygen columns (Figure 1f), indicating the fluorite-like oxygen arrangement (Figure 1g) with a random distribution of oxygen vacancies at the atomic scale. In other words, the material is in an intermediate state between pyrochlore and fluorite structures, comprising a random mix of nanoscale pyrochlore and vacancy-rich fluorite phases. XRD analysis was also performed (Figure S5). However, the XRD pattern exhibits four identical peaks similar to those of both fluorite CeO_2 and pyrochlore $Ce_2Zr_2O_7$, making it challenging to determine the exact crystal structures of the HEO NPs. Selected area electron diffraction (SAED) analysis was then performed on the HEO NPs (Figure S6), capturing the large *d*-spacing planes characteristic of pyrochlore {111} planes, thus confirming the existence of the pyrochlore phase. Since both phases can accommodate a wide range of oxygen vacancies, the HEO NPs should host numerous oxygen vacancies without lattice collapse, which is expected to facilitate migration of oxygen vacancies and atoms during catalytic reactions involving the Mars–van Krevelen mechanism,[30,31] such as emission control catalysis, hydrocarbon reforming, and alcohol oxidation. The presence of this intermediate structural state may be attributed to several factors: the presence of aliovalent cations and differences in the atomic radii of the elements, nonequilibrium synthesis conditions, and the pseudorandom distribution of aliovalent cations[32,33] (Supporting Note I).

Various STEM techniques were combined to elucidate the atomic scale structure and chemistry of HEO surfaces. Figure 2a shows the HAADF-STEM and corresponding EDX analysis at the surface region of the as-synthesized NP along the [1$\bar{1}$0] direction (the first four surface layers are marked). Away from the surface, the alternate occupancy of Ce and Y with Hf and Ti can be clearly visualized in the EDX maps (Figure 2a) and the corresponding intensity profile (Figure S7) across the surface (yellow arrow). This is identical to the bulk structure, as discussed earlier. However, the outmost surface monolayer shows a clear chemical reconstruction and is elementally dissimilar to the particle bulk: first, the outmost surface layer is terminated with a B site (Ti and Hf) rich plane, while the Hf signal is almost negligible compared to Ti in this layer. Distinct Ce, La, and Ti signals are observed in the top layer of the elemental maps as well as in the intensity line profile (Figure S7), while there is a negligible contribution from the other elements of the HEO. Second, Ce, La, and Ti are populated at all atom locations in the first atom layer (line profile along the surface layer (Figure S8)), unlike the preferred alternative distribution in the bulk. Figure S9 shows another surface region from a different particle, where similar cation arrangements from surface to subsurface were observed. The EDX line profile also reveals the enrichment of Ce, La, and Ti at the outermost surface of the HEO (Figure S10). These findings suggest that the observed cation distributions are common in HEO NPs.

The structural and chemical analyses of the pristine HEO NP provide a basis for tracking its surface evolution under catalytic conditions. Since HEO NPs are believed to excel in high-temperature reactions due to their stability, we performed ex situ redox treatments on the NPs. First, they were exposed to a 4% H_2–Ar reduction environment at 650 °C for 2 h. No significant chemical segregation occurred (Figure S11). Subsequent STEM imaging of the surface region (Figure 3) revealed that the subsurface and bulk crystal structures were unaffected by the reduction treatment. However, the cation arrangement at the first atom layer observed in the pristine phase is no longer present. Instead, the outmost surface atom layer adopts a {111} pyrochlore structure, consistent with the subsurface atomic arrangement. These interesting transitions are evidenced by the corresponding atomic-scale elemental maps (first four surface layers marked): (1) the surface monolayer shows a clear loss of Ce compared to the pristine structure, as indicated by the much weaker Ce peak of the first layer in the intensity line profile (Figure S12, red arrow); (2) the intensity line profile of the first surface atom layer (Figure S13) displays an apparent ordered configuration, where Ce

https://doi.org/10.1021/acs.nanolett.4c02985
Nano Lett. XXXX, XXX, XXX−XXX

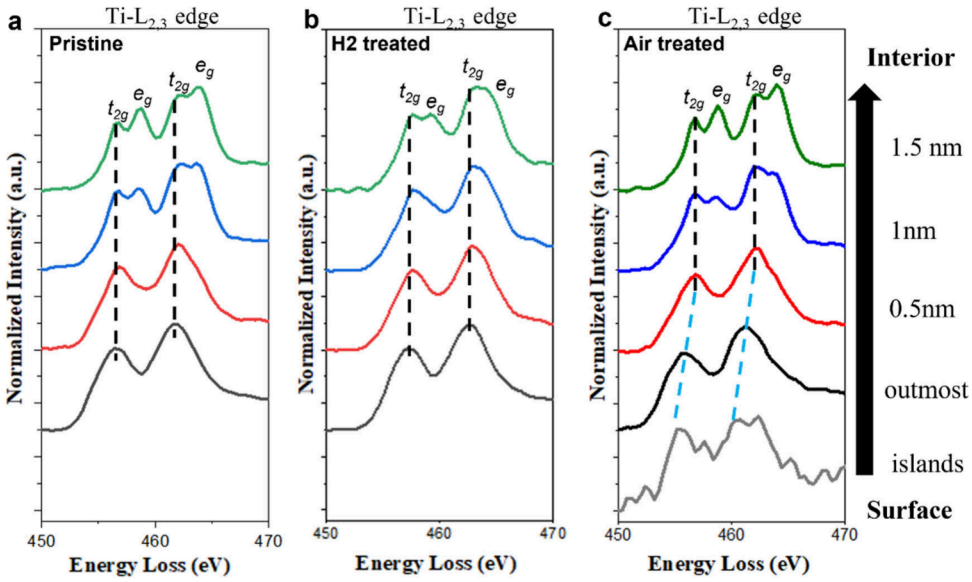

Figure 5. EELS line-scan analysis of Ti L edges from the surface to the bulk in HEO particles after different treatments. EELS profile of the Ti $L_{2,3}$ peaks of HEO (a) in pristine condition, (b) after H_2 treatment, and (c) after air treatment.

peaks alternate with Ti ones along the first atomic layer (marked by cyan and orange arrows, respectively), while La remains unaffected and evenly distributed. Compared to the pristine random elemental distribution, the surface layer exhibits a disorder to order transformation due to the reduction heat treatment; Thus, the reduction of HEO NPs drives the ordering of elements at the surface to a certain extent.

Upon subjecting the pristine HEO NPs to air treatment at 650 °C for 2 h, no noticeable chemical inhomogeneity was observed (Figure S14). The overall crystal structure remains intact, while the elemental distributions undergo significant changes (Figure 4, first four surface layers marked). Elements Y, Zr, and Hf tend to migrate to the surface, as revealed by the intensity line profiles from the surface into the bulk in Figure S15, resulting in the presence of all six elements at the surface monolayer (red arrow). This contrasts with the pristine surface structure, which consisted of only Ti, La, and Ce columns. The high-temperature oxygen-rich environment appears to drive elements from the bulk to the surface, which is the opposite effect of the heat treatment. Hf undergoes a drastic change: it had the highest occupancy at the B sites in the pristine structure. After the oxidation heat treatment, it migrates to adjacent sites and becomes well distributed in all atomic columns, as shown in Figure S15, where noticeable Hf signals are observed on all atomic layers (black arrows). The redistribution behavior of Hf also demonstrates a slight chemical order-to-disorder transformation at the surface and subsurface of the particle. Interestingly, atomic islands on the surface (circled in the STEM image) composed mostly of Ti and La cations (marked by a gray arrow in the intensity profile) are observed. It is worth noticing the presence of Ti/La oxide islands at the outmost surface (Figure S16a). Unexpectedly, the atomic arrangement of the islands does not follow the bulk crystal structure. The atom layer spacing and lattice symmetry of the islands (Figure S16b and S16c) suggest that these islands resemble a perovskite-like structure, i.e., $LaTiO_{3-x}$ with {110} as surface planes. A slightly larger layer spacing between the first and the second layer (2.89 Å vs 2.69 Å) suggests the possibility of the adsorption of oxygen gas molecules.[34] Such surface atomic islands contain a significant number of uncoordinated sites and oxygen vacancies,[35,36] which can facilitate tunable reduction−oxidation and acid−base properties, enabling selective adsorption of reactants and serving as anchoring sites for durable atomically dispersed catalysts.[35,37,38] Long time higher temperature treatment (900 °C for 5 h in Ar) was also performed on the HEO NPs to see their evolutions (details in Supporting Note II).

To investigate the atomic rearrangement on HEO surfaces under redox conditions, we constructed surface models of HEO in pyrochlore and fluoride structures (Figure S17), as well as reduced (Figure S18) and oxidized (Figure S19) HEO surface structures, based on experimental STEM-EDX analysis (elemental maps as discussed previously and elemental quantifications in Figure S20 and Table S1). The cation-exchange energetics were computed using DFT, and the details can be found in the SI. Our analysis, as summarized in Table S2 and Figure S21, reveals the energies of elemental migrations during redox gas conditions (Supporting Note III).

A common observation across different environments is the presence of Ti cations in the surface and subsurface regions of the HEO NPs. The coordination and valence state of Ti strongly influence the HEO NPs' surface electronic structure and catalytic performance. STEM-electron energy loss spectroscopy (EELS) was used to study the Ti valence state under various redox environments. Figure 5 presents EELS profiles of the Ti $L_{2,3}$ edges as the probe moves from the surface to the bulk with a 0.5 nm step size. In pristine HEO NPs, bulk Ti has a valence of $\sim 4^+$ with clear t_{2g} and e_g splits, while surface Ti has a lower valence of $\sim 3^+$ based on merging split peaks and energy shifts[39,40] (Figure 5a). The thickness of the reduced surface layer is about 1−1.5 nm. Surprisingly, a 4% H_2-650 °C environment does not further reduce surface Ti^{3+} but reduces Ti^{4+} beneath the surface, thereby increasing the depth of the surface reducing layer (Figure 5b). A clear reduction to Ti^{3+} is observed at ∼1.5 nm from the surface and subsurface regions, indicating the abundance of oxygen vacancies. The oxidation environment induces distinct changes in surface Ti coordination and valence states on the surface (Figure 5c), confirming the formation of $LaTiO_{3-x}$-like islands observed in our imaging

https://doi.org/10.1021/acs.nanolett.4c02985
Nano Lett. XXXX, XXX, XXX−XXX

and mapping. These sites can also directly participate in activating reactants or act as stable anchoring sites for metal species in heterogeneous catalysis.[35,41]

Our STEM imaging and spectroscopy analysis demonstrate the abundant presence of oxygen vacancies at high temperatures, irrespective of redox environments. This experimental evidence provides a good explanation for the HEOs in various applications in which oxygen vacancies and structural stability are critical factors. For instance, HEOs exhibit outstanding catalytic activity in reactions such as partial oxidation, water−gas shift, methane reforming, and CO_2 conversion,[2,42] where oxygen vacancies promote reactions by increasing the mobility of oxygen ions and facilitating the transfer of oxygen atoms. In energy storage applications, HEOs have recently demonstrated exceptional capacity retention as electrodes in alkali ion batteries; while their thermal and structural stability were highlighted as the main contributing factors,[5,13,15] our findings suggest that the abundant oxygen vacancies in HEOs may also contribute significantly to their performance, since the presence of oxygen vacancies has the potential to enhance the mobility of lithium ions and serve as active sites for redox reactions.[43−45] Our findings explain the value of HEOs in energy storage and catalysis, highlighting the importance of understanding surface characteristics in HEO particles, particularly under their operation conditions, for the design of HEOs in energy applications. The atomic arrangements and elemental distributions revealed in this study also provide direct input for structural calculations.

■ ASSOCIATED CONTENT

Supporting Information

The Supporting Information is available free of charge at https://pubs.acs.org/doi/10.1021/acs.nanolett.4c02985.

Experimental Methods, additional STEM imaging and mapping analysis, and DFT modeling (PDF)

■ AUTHOR INFORMATION

Corresponding Authors

Liangbing Hu − *Department of Materials Science and Engineering, University of Maryland, College Park, Maryland 20742, United States;* orcid.org/0000-0002-9456-9315; Email: binghu@umd.edu

Zili Wu − *Chemical Sciences Division, Oak Ridge National Laboratory, Oak Ridge, Tennessee 37831, United States;* orcid.org/0000-0002-4468-3240; Email: wuz1@ornl.gov

De-en Jiang − *Department of Chemical and Biomolecular Engineering, Vanderbilt University, Nashville, Tennessee 37235, United States;* orcid.org/0000-0001-5167-0731; Email: de-en.jiang@vanderbilt.edu

Miaofang Chi − *Center of Nanophase Materials Science, Oak Ridge National Laboratory, Oak Ridge, Tennessee 37831, United States; Mechanical Engineering and Materials Science, Duke University, Durham, North Carolina 27708, United States;* orcid.org/0000-0003-0764-1567; Email: chim@ornl.gov

Authors

Zhennan Huang − *Center of Nanophase Materials Science, Oak Ridge National Laboratory, Oak Ridge, Tennessee 37831, United States; Department of Materials Science and Engineering, University of Maryland, College Park, Maryland 20742, United States*

Lu Wang − *Department of Chemistry, University of California, Riverside, California 92521, United States*

Tangyuan Li − *Department of Materials Science and Engineering, University of Maryland, College Park, Maryland 20742, United States;* orcid.org/0009-0001-1232-0613

Kartik Venkatraman − *Center of Nanophase Materials Science, Oak Ridge National Laboratory, Oak Ridge, Tennessee 37831, United States*

Yang He − *Chemical Sciences Division, Oak Ridge National Laboratory, Oak Ridge, Tennessee 37831, United States*

Felipe Polo-Garzon − *Chemical Sciences Division, Oak Ridge National Laboratory, Oak Ridge, Tennessee 37831, United States;* orcid.org/0000-0002-6507-6183

Jacob Smith − *Center of Nanophase Materials Science, Oak Ridge National Laboratory, Oak Ridge, Tennessee 37831, United States*

Yiheng Du − *Department of Materials Science and Engineering, University of Maryland, College Park, Maryland 20742, United States*

Complete contact information is available at: https://pubs.acs.org/10.1021/acs.nanolett.4c02985

Author Contributions

Conceptualization: M.C. and Z.W. Material production: T.L. and L.H. Electron microscopy: Z.H., J.S., and M.C. First-principles calculations: L.W. and D.J.. Data analysis and interpretation: Z.H., L.W., T.L., K.V., Y.H., F.P.-G., J.S., Y.D., Z.W., D.J., L.H., M.C. Funding acquisition and supervision: Z.W., D.J., L.H., M.C. Writing−review and editing: All authors reviewed and edited the manuscript.

Notes

The authors declare no competing financial interest.

This manuscript has been authored by UT-Battelle, LLC, under Contract No. DE-AC0500OR22725 with the U.S. Department of Energy. The United States Government retains and the publisher, by accepting the article for publication, acknowledges that the United States Government retains a nonexclusive, paid-up, irrevocable, worldwide license to publish or reproduce the published form of this manuscript, or allow others to do so, for the United States Government purposes. The Department of Energy will provide public access to these results of federally sponsored research in accordance with the DOE Public Access Plan (http://energy.gov/downloads/doe-public-access-plan).

■ ACKNOWLEDGMENTS

Research was sponsored by the US DOE, Office of Science, Office of Basic Energy Sciences (BES), Chemical Sciences, Geosciences, and Biosciences Division, Catalysis Science program. Technique development and data analysis were supported by U.S. DOE Office of Science under Early Career award no. ERKCZ55. Microscopy experiments were conducted at the Center for Nanophase Materials Sciences (CNMS), which is a U.S. Department of Energy, Office of Science User Facility at Oak Ridge National Laboratory. Liangbing Hu acknowledges the financial support from the U.S. Department of Energy, Office of Science, Basic Energy Sciences under Award No. DE-SC0023357 and the U.S. Department of Energy, Office of Science Energy Earthshot Initiative as part of the Non-equilibrium Energy Transfer for Efficient Reactions

(NEETER) at Oak Ridge National Laboratory under contract #DE-AC05-00OR22725.

REFERENCES

(1) Li, T.; Yao, Y.; Huang, Z.; Xie, P.; Liu, Z.; Yang, M.; Gao, J.; Zeng, K.; Brozena, A. H.; Pastel, G.; others. Denary Oxide Nanoparticles as Highly Stable Catalysts for Methane Combustion. *Nature Catalysis* **2021**, *4* (1), 62−70.
(2) Sun, Y.; Dai, S. High-Entropy Materials for Catalysis: A New Frontier. *Science Advances* **2021**, *7* (20), 1−24.
(3) Oses, C.; Toher, C.; Curtarolo, S. High-Entropy Ceramics. *Nature Reviews Materials* **2020**, *5* (4), 295−309.
(4) Sarkar, A.; Velasco, L.; Wang, D.; Wang, Q.; Talasila, G.; De Biasi, L.; Kübel, C.; Brezesinski, T.; Bhattacharya, S. S.; Hahn, H.; Breitung, B. High Entropy Oxides for Reversible Energy Storage. *Nat. Commun.* **2018**, *9* (1), 3400.
(5) Lun, Z.; Ouyang, B.; Kwon, D. H.; Ha, Y.; Foley, E. E.; Huang, T. Y.; Cai, Z.; Kim, H.; Balasubramanian, M.; Sun, Y.; Huang, J.; Tian, Y.; Kim, H.; McCloskey, B. D.; Yang, W.; Clément, R. J.; Ji, H.; Ceder, G. Cation-Disordered Rocksalt-Type High-Entropy Cathodes for Li-Ion Batteries. *Nat. Mater.* **2021**, *20* (2), 214−221.
(6) Sarkar, A.; Wang, Q.; Schiele, A.; Chellali, M. R.; Bhattacharya, S. S.; Wang, D.; Brezesinski, T.; Hahn, H.; Velasco, L.; Breitung, B. High-Entropy Oxides: Fundamental Aspects and Electrochemical Properties. *Adv. Mater.* **2019**, *31* (26), No. 1806236.
(7) Cao, G.; Liang, J.; Guo, Z.; Yang, K.; Wang, G.; Wang, H.; Wan, X.; Li, Z.; Bai, Y.; Zhang, Y.; Liu, J.; Feng, Y.; Zheng, Z.; Lu, C.; He, G.; Xiong, Z.; Liu, Z.; Chen, S.; Guo, Y.; Zeng, M.; Lin, J.; Fu, L. Liquid Metal for High-Entropy Alloy Nanoparticles Synthesis. *Nature* **2023**, *619* (7968), 73−77.
(8) Banko, L.; Tetteh, E. B.; Kostka, A.; Piotrowiak, T. H.; Krysiak, O. A.; Hagemann, U.; Andronescu, C.; Schuhmann, W.; Ludwig, A. Microscale Combinatorial Libraries for the Discovery of High-Entropy Materials. *Adv. Mater.* **2023**, *35* (9), No. 2207635.
(9) Katzbaer, R. R.; Dos Santos Vieira, F. M.; Dabo, I.; Mao, Z.; Schaak, R. E. Band Gap Narrowing in a High-Entropy Spinel Oxide Semiconductor for Enhanced Oxygen Evolution Catalysis. *J. Am. Chem. Soc.* **2023**, *145* (12), 6753−6761.
(10) Kumbhakar, M.; Khandelwal, A.; Jha, S. K.; Kante, M. V.; Keßler, P.; Lemmer, U.; Hahn, H.; Aghassi-Hagmann, J.; Colsmann, A.; Breitung, B.; Velasco, L.; Schweidler, S. High-Throughput Screening of High-Entropy Fluorite-Type Oxides as Potential Candidates for Photovoltaic Applications. *Adv. Energy Mater.* **2023**, *13* (24), No. 2204337.
(11) Aamlid, S. S.; Oudah, M.; Rottler, J.; Hallas, A. M. Understanding the Role of Entropy in High Entropy Oxides. *J. Am. Chem. Soc.* **2023**, *145* (11), 5991−6006.
(12) Divilov, S.; Eckert, H.; Hicks, D.; Oses, C.; Toher, C.; Friedrich, R.; Esters, M.; Mehl, M. J.; Zettel, A. C.; Lederer, Y.; Zurek, E.; Maria, J.-P.; Brenner, D. W.; Campilongo, X.; Filipović, S.; Fahrenholtz, W. G.; Ryan, C. J.; DeSalle, C. M.; Crealese, R. J.; Wolfe, D. E.; Calzolari, A.; Curtarolo, S. Disordered Enthalpy−Entropy Descriptor for High-Entropy Ceramics Discovery. *Nature* **2024**, *625* (7993), 66−73.
(13) Zhang, R.; Wang, C.; Zou, P.; Lin, R.; Ma, L.; Yin, L.; Li, T.; Xu, W.; Jia, H.; Li, Q.; Sainio, S.; Kisslinger, K.; Trask, S. E.; Ehrlich, S. N.; Yang, Y.; Kiss, A. M.; Ge, M.; Polzin, B. J.; Lee, S. J.; Xu, W.; Ren, Y.; Xin, H. L. Compositionally Complex Doping for Zero-Strain Zero-Cobalt Layered Cathodes. *Nature* **2022**, *610* (7930), 67−73.
(14) Zhao, C.; Ding, F.; Lu, Y.; Chen, L.; Hu, Y. S. High-Entropy Layered Oxide Cathodes for Sodium-Ion Batteries. *Angewandte Chemie - International Edition* **2020**, *59* (1), 264−269.
(15) Yao, L.; Zou, P.; Wang, C.; Jiang, J.; Ma, L.; Tan, S.; Beyer, K. A.; Xu, F.; Hu, E.; Xin, H. L. High-Entropy and Superstructure-Stabilized Layered Oxide Cathodes for Sodium-Ion Batteries. *Adv. Energy Mater.* **2022**, *12* (41), 1−9.
(16) Wang, K.; Hua, W.; Huang, X.; Stenzel, D.; Wang, J.; Ding, Z.; Cui, Y.; Wang, Q.; Ehrenberg, H.; Breitung, B.; Kübel, C.; Mu, X. Synergy of Cations in High Entropy Oxide Lithium Ion Battery Anode. *Nat. Commun.* **2023**, *14* (1), 1487.
(17) Wang, Y.; Robson, M. J.; Manzotti, A.; Ciucci, F. High-Entropy Perovskites Materials for next-Generation Energy Applications. *Joule* **2023**, *7* (5), 848−854.
(18) Xu, H.; Zhang, Z.; Liu, J.; Do-Thanh, C. L.; Chen, H.; Xu, S.; Lin, Q.; Jiao, Y.; Wang, J.; Wang, Y.; Chen, Y.; Dai, S. Entropy-Stabilized Single-Atom Pd Catalysts via High-Entropy Fluorite Oxide Supports. *Nat. Commun.* **2020**, *11* (1), 1−9.
(19) Kante, M. V.; Weber, M. L.; Ni, S.; van den Bosch, I. C. G.; van der Minne, E.; Heymann, L.; Falling, L. J.; Gauquelin, N.; Tsvetanova, M.; Cunha, D. M.; Koster, G.; Gunkel, F.; Nemšák, S.; Hahn, H.; Velasco Estrada, L.; Baeumer, C. A High-Entropy Oxide as High-Activity Electrocatalyst for Water Oxidation. *ACS Nano* **2023**, *17* (6), 5329−5339.
(20) Pan, Y.; Liu, J. X.; Tu, T. Z.; Wang, W.; Zhang, G. J. High-Entropy Oxides for Catalysis: A Diamond in the Rough. *Chemical Engineering Journal* **2023**, *451* (P2), 138659−138659.
(21) Li, T.; Yao, Y.; Ko, B. H.; Huang, Z.; Dong, Q.; Gao, J.; Chen, W.; Li, J.; Li, S.; Wang, X.; Shahbazian-Yassar, R.; Jiao, F.; Hu, L. Carbon-Supported High-Entropy Oxide Nanoparticles as Stable Electrocatalysts for Oxygen Reduction Reactions. *Adv. Funct. Mater.* **2021**, *31* (21), No. 2010561.
(22) Zeng, Y.; Ouyang, B.; Liu, J.; Byeon, Y.-W.; Cai, Z.; Miara, L. J.; Wang, Y.; Ceder, G. High-Entropy Mechanism to Boost Ionic Conductivity. *Science* **2022**, *378* (6626), 1320−1324.
(23) Zheng, W.; Liang, G.; Liu, Q.; Li, J.; Yuwono, J. A.; Zhang, S.; Peterson, V. K.; Guo, Z. The Promise of High-Entropy Materials for High-Performance Rechargeable Li-Ion and Na-Ion Batteries. *Joule* **2023**, *7* (12), 2732−2748.
(24) Yang, B.; Zhang, Y.; Pan, H.; Si, W.; Zhang, Q.; Shen, Z.; Yu, Y.; Lan, S.; Meng, F.; Liu, Y.; Huang, H.; He, J.; Gu, L.; Zhang, S.; Chen, L. Q.; Zhu, J.; Nan, C. W.; Lin, Y. H. High-Entropy Enhanced Capacitive Energy Storage. *Nat. Mater.* **2022**, *21* (9), 1074−1080.
(25) Jiang, S.; Hu, T.; Gild, J.; Zhou, N.; Nie, J.; Qin, M.; Harrington, T.; Vecchio, K.; Luo, J. A New Class of High-Entropy Perovskite Oxides. *Scripta Materialia* **2018**, *142*, 116−120.
(26) Yao, Y.; Huang, Z.; Xie, P.; Lacey, S. D.; Jacob, R. J.; Xie, H.; Chen, F.; Nie, A.; Pu, T.; Rehwoldt, M.; Yu, D.; Zachariah, M. R.; Wang, C.; Shahbazian-Yassar, R.; Li, J.; Hu, L. Carbothermal Shock Synthesis of High-Entropy-Alloy Nanoparticles. *Science* **2018**, *359* (6383), 1489−1494.
(27) Ding, Q.; Zhang, Y.; Chen, X.; Fu, X.; Chen, D.; Chen, S.; Gu, L.; Wei, F.; Bei, H.; Gao, Y.; Wen, M.; Li, J.; Zhang, Z.; Zhu, T.; Ritchie, R. O.; Yu, Q. Tuning Element Distribution, Structure and Properties by Composition in High-Entropy Alloys. *Nature* **2019**, *574* (7777), 223−227.
(28) Su, L.; Huyan, H.; Sarkar, A.; Gao, W.; Yan, X.; Addiego, C.; Kruk, R.; Hahn, H.; Pan, X. Direct Observation of Elemental Fluctuation and Oxygen Octahedral Distortion-Dependent Charge Distribution in High Entropy Oxides. *Nat. Commun.* **2022**, *13* (1), 2358−2358.
(29) Marlton, F. P.; Zhang, Z.; Zhang, Y.; Proffen, T. E.; Ling, C. D.; Kennedy, B. J. Lattice Disorder and Oxygen Migration Pathways in Pyrochlore and Defect-Fluorite Oxides. *Chem. Mater.* **2021**, *33* (4), 1407−1415.
(30) Ferreira De Araújo, J.; Dionigi, F.; Merzdorf, T.; Oh, H.; Strasser, P. Evidence of Mars-Van-Krevelen Mechanism in the Electrochemical Oxygen Evolution on Ni-Based Catalysts. *Angew. Chem.* **2021**, *133* (27), 15108−15115.
(31) Mars, P.; Van Krevelen, D. W. Oxidations Carried out by Means of Vanadium Oxide Catalysts. *Chem. Eng. Sci.* **1954**, *3*, 41−59.
(32) Ji, Q.; Bi, L.; Zhang, J.; Cao, H.; Zhao, X. S. The Role of Oxygen Vacancies of ABO3perovskite Oxides in the Oxygen Reduction Reaction. *Energy Environ. Sci.* **2020**, *13* (5), 1408−1428.
(33) Papac, M.; Stevanović, V.; Zakutayev, A.; O'Hayre, R. Triple Ionic−Electronic Conducting Oxides for next-Generation Electrochemical Devices. *Nat. Mater.* **2021**, *20* (3), 301−313.

https://doi.org/10.1021/acs.nanolett.4c02985
Nano Lett. XXXX, XXX, XXX−XXX

(34) Yoshida, H.; Kuwauchi, Y.; Jinschek, J. R.; Sun, K.; Kohyama, M.; Shimada, S.; Haruta, M.; Takeda, S. Visualizing Gas Molecules Interacting with Supported Nanoparticulate Catalysts at Reaction Conditions. *Science* **2012**, *335* (6066), 317−319.
(35) Li, X.; Pereira-Hernández, X. I.; Chen, Y.; Xu, J.; Zhao, J.; Pao, C. W.; Fang, C. Y.; Zeng, J.; Wang, Y.; Gates, B. C.; Liu, J. Functional CeOx Nanoglues for Robust Atomically Dispersed Catalysts. *Nature* **2022**, *611* (7935), 284−288.
(36) Shen, Y.; Ren, C.; Zheng, L.; Xu, X.; Long, R.; Zhang, W.; Yang, Y.; Zhang, Y.; Yao, Y.; Chi, H.; Wang, J.; Shen, Q.; Xiong, Y.; Zou, Z.; Zhou, Y. Room-Temperature Photosynthesis of Propane from CO2 with Cu Single Atoms on Vacancy-Rich TiO2. *Nat. Commun.* **2023**, *14* (1), 1117.
(37) Yi, Z.; Lin, L.; Chang, Y.; Luo, X.; Gao, J.; Mu, R.; Ning, Y.; Fu, Q.; Bao, X. Dynamic Transformation between Bilayer Islands and Dinuclear Clusters of Cr Oxide on Au(111) through Environment and Interface Effects. *Proc. Natl. Acad. Sci. U.S.A.* **2022**, *119* (22), 1−7.
(38) Freund, H. J. Clusters and Islands on Oxides: From Catalysis via Electronics and Magnetism to Optics. *Surf. Sci.* **2002**, *500* (1−3), 271−299.
(39) Sun, R.; Wang, Z.; Saito, M.; Shibata, N.; Ikuhara, Y. Atomistic Mechanisms of Nonstoichiometry-Induced Twin Boundary Structural Transformation in Titanium Dioxide. *Nat. Commun.* **2015**, *6* (1), 7120.
(40) Susarla, S.; García-Fernández, P.; Ophus, C.; Das, S.; Aguado-Puente, P.; McCarter, M.; Ercius, P.; Martin, L. W.; Ramesh, R.; Junquera, J. Atomic Scale Crystal Field Mapping of Polar Vortices in Oxide Superlattices. *Nat. Commun.* **2021**, *12* (1), 1−7.
(41) Yang, P.; Pan, J.; Liu, Y.; Zhang, X.; Feng, J.; Hong, S.; Li, D. Insight into the Role of Unsaturated Coordination O_{2c}-Ti_{5c}-O_{2c} Sites on Selective Glycerol Oxidation over $AuPt/TiO_2$ Catalysts. *ACS Catal.* **2019**, *9* (1), 188−199.
(42) Svane, K. L.; Rossmeisl, J. Theoretical Optimization of Compositions of High-Entropy Oxides for the Oxygen Evolution Reaction**. *Angew. Chem. Int. Ed* **2022**, *61* (19), No. e202201146.
(43) Kim, H.-S.; Cook, J. B.; Lin, H.; Ko, J. S.; Tolbert, S. H.; Ozolins, V.; Dunn, B. Oxygen Vacancies Enhance Pseudocapacitive Charge Storage Properties of MoO3−x. *Nat. Mater.* **2017**, *16* (4), 454−460.
(44) Zhang, A.; Gao, R.; Hu, L.; Zang, X.; Yang, R.; Wang, S.; Yao, S.; Yang, Z.; Hao, H.; Yan, Y.-M. Rich Bulk Oxygen Vacancies-Engineered MnO2 with Enhanced Charge Transfer Kinetics for Supercapacitor. *Chemical Engineering Journal* **2021**, *417*, No. 129186.
(45) Li, L.; Meng, T.; Wang, J.; Mao, B.; Huang, J.; Cao, M. Oxygen Vacancies Boosting Lithium-Ion Diffusion Kinetics of Lithium Germanate for High-Performance Lithium Storage. *ACS Appl. Mater. Interfaces* **2021**, *13* (21), 24804−24813.

https://doi.org/10.1021/acs.nanolett.4c02985
Nano Lett. XXXX, XXX, XXX−XXX